

Experimental Study of Aqueous Humor Flow in a Transparent Anterior Segment Phantom by Using PIV Technique

Wenjia Wang^{1,2}, Xiuqing Qian^{1,2}, Qi Li^{1,2}, Gong Zhang^{1,2}, Huangxuan Zhao^{1,2}, Tan Li^{1,2}, Yang Yu^{1,2}, Hongfang Song^{1,2,*} and Zhicheng Liu^{1,2,*}

Abstract: Pupillary block is considered as an important cause of primary angle-closure glaucoma (PACG). In order to investigate the effect of pupillary block on the hydrodynamics of aqueous humor (AH) in anterior chamber (AC) and potential risks, a 3D printed eye model was developed to mimic the AH flow driven by fluid generation, the differential pressure between AC and posterior chambers (PC) and pupillary block. Particle image velocimetry technology was applied to visualize flow distribution. The results demonstrated obvious differences in AH flow with and without pupillary block. Under the normal condition (without pupillary block), the flow field of AH was nearly symmetric in the AC. The highest flow velocity located at the central of AC when the differential pressure between AC and PC was under 5.83 Pa, while it appeared near the cornea and iris surface when the differential pressure was greater than 33.6 Pa. Once pupillary block occurred, two asymmetric vortices with different sizes were observed and the shear stress in the paracentral cornea and iris epithelium increased greatly. It can be concluded that the pupillary block and the elevated differential pressure between AC and PC could change the flow distribution and thus increase the risk of corneal endothelial cells detachment. This study could make a further understanding of the pathogenesis of PACG.

Keywords: Aqueous humor, particle image velocimetry, experimental flow visualization, glaucoma.

1 Introduction

Glaucoma is the leading cause of incurable blindness worldwide [Sena and Lindsley (2013); Weinreb, Aung and Medeiros (2014); Congdon and Friedman (2003); Pascolini and Mariotti (2012)]. The primary risk factor for glaucoma is the elevation of intraocular pressure (IOP), which could cause the progressive damage to the structure and function of optic nerve [Ethier, Johnson and Ruberti (2004)]. Primary angle-closure glaucoma

¹ School of Biomedical Engineering, Capital Medical University, Beijing, China.

² Beijing Key Laboratory of Fundamental Research on Biomechanics in Clinical Application, Beijing, China.

* Corresponding Authors: Zhicheng Liu. Email: zcliu@ccmu.edu.cn;

Hongfang Song. Email: songhf@ccmu.edu.cn.

(PACG) is one of the common subtypes of glaucoma, with a particularly high prevalence (about three quarters) in Asia [Chan, Li, Tham et al. (2016); Tham, Hons, Li et al. (2014)]. It is associated with the appositional or synechial closure of the anterior chamber (AC) angle (between the iris and the corneoscleral shell [Huang and Barocas (2004)], leading to the anterior protrusion of iris and further increase of IOP.

The generation and outflow of aqueous humor (AH) is essential to keep the balance of IOP [Huang, Francis and Weinreb (2017)] and supply nutrition to avascular ocular tissues [Caprioli (1992); Fontana and Brubaker (1980)]. AH is a transparent fluid and has similar rheological properties to water. It is secreted by ciliary body continuously, flows from posterior chamber (PC) into anterior chamber (AC) through the pupil and drains through trabecular meshwork (Fig. 1). Previous study has demonstrated that pupillary block was the main cause of PACG [Barkan (1954)]. It could lead to abnormal flow of AH, resulting in obvious increase of differential pressure between AC and PC. The elevation of the differential pressure could push the iris anteriorly and further narrow the AC angle, which eventually cause the irreversible damage to the optic nerve [Quigley, Friedman and Congdon (2003)]. However, the effect of pupillary block on the fluid dynamics of AH in the AC is still not clear, and the potential risks of changed AH flow need to be further evaluated.

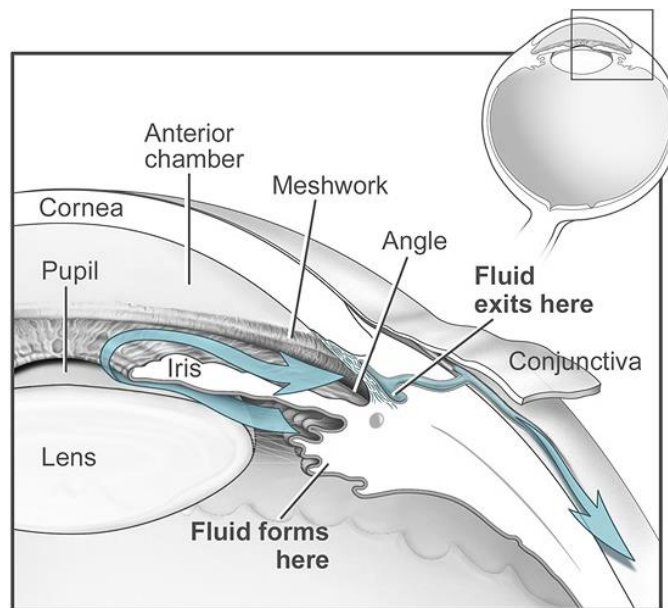


Figure 1: Diagram of the anterior segment of eye [National Eye Institute (2012)]

Due to the small size of AC and the complexity of flow measurements, it is difficult to conduct measurement in real eyes. There are two alternatives to obtain fluid data close to the real situation. One approach is the computational flow analysis, which can quickly simulate the fluid flow at low cost, and has been applied to simulate the flow of AH in AC [Avtar and Srivastava (2014); Olkhovskiy and Friedmann (2017); Repetto, Pralits, Siggers (2015); Wessapan and Rattanadecho (2014); Villamarin, Roy, Hasballa et al. (2012)]. However, this technique is based on the given boundary conditions and

theoretical assumptions, and the accuracy of the simulation results still needs further verification. The other approach is experimental fluid analysis. The most advanced experimental technology of fluid mechanics is particle image velocimetry (PIV) and it is often employed to verify the simulation results. Due to the limitation of model accuracy, traditional PIV is not suitable for studying fluid flow in complex tissues and organs. 3D printing technology can compensate for this deficiency. Previous studies have demonstrated the feasibility and accuracy of PIV combined with 3D printing for biofluid flow simulation [Aycock, Hariharan and Craven (2017); Scardulla, Bellavia, D'Acquisto et al. (2017); Hong, Ji, Kim et al. (2017); Kaesler, Schlanstein, Hesselmann et al. (2017)]. However, the flow visualization in these studies was conducted with high flow rates. The application of this method to visualize a low speed flow (e.g., the AH flow in AC) has not been reported.

The purpose of this study was to reveal the hydrodynamics of AH in AC and to analyze the effect of pupillary block on fluid distribution and its corresponding potential risks, which could provide the scientific basis for the pathogenesis of PACG.

2 Material and methods

An enlarged eye model was printed out by 3D printing technology based on the similitude theory. Then the AH hydrodynamic characteristics under various differential pressures between AC and PC were studied by PIV experiment. Finally, the differences of AH flow distribution between normal and pupil obstruction were compared and the possible risks were discussed.

2.1 PIV model

A fully transparent model of human eye is essential for the PIV experiment. In order to increase spatial resolution and overall image quality, a PIV model scaled up by 5 times compared to the original size was designed. The PIV model was developed from the typical ocular dimensions and then manufactured by 3D printing technology to obtain a rigid, transparent flow pathway of fluid. The geometry of the model has been described in our previous study [Wang, Qian, Song et al. (2016)].

For the sake of preserving the geometry of flow field, the PIV model was improved and manufactured as Fig. 2. Two rings, representing the respective production channels and drainage channels ((8) and (9) in Fig. 2(c)), were installed in the model, which simulated the ciliary body and collector channels. The model was composed of five parts, including cornea, iris, lens, bottom and foils (Fig. 2(a)). Screws and bolts were fastened to seal off all parts of the model. Besides, the bottom part of the model was made of solid polymethyl methacrylate (PMMA) to eliminate the interference of instability in the PIV experiment. Furthermore, the gap between iris and lens was adjustable by inserting four pieces of foils (0.1mm thickness) under the column of lens to simulate pupillary block [Barocas and Huang (2004)].

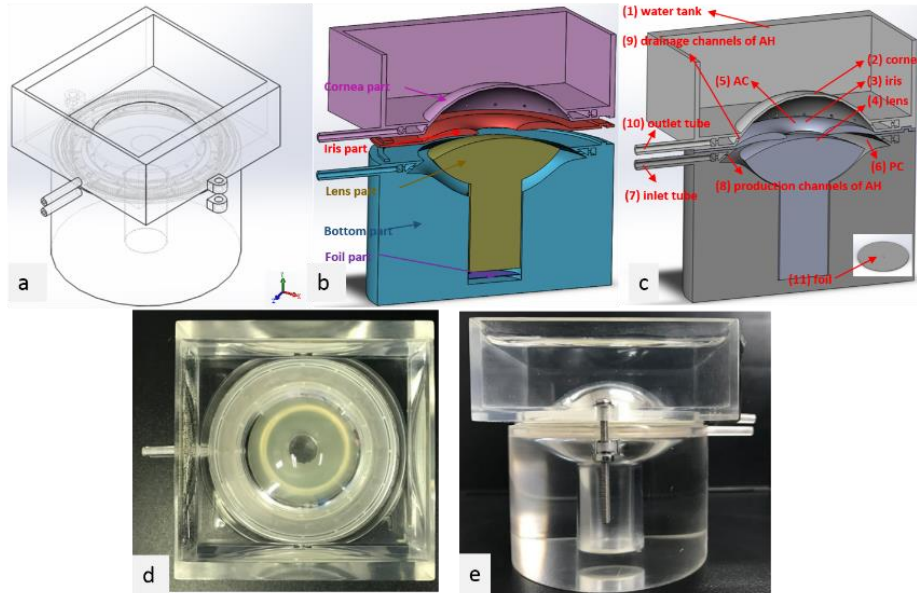


Figure 2: The scheme (a-c) and pictures (d-e) of PIV model, containing water tank (1), cornea (2), iris (3), lens (4), AC (5), PC (6), inlet tube (7), production channels of AH (8), drainage channels of AH (9) and outlet tube (10). The 0.1 mm thickness foils (11) could be insert under the column of lens to reduce the gap between the iris and lens

2.2 AH generation simulation

Normal saline resolution was used in the PIV model to simulate the AH flow, resulting in the same mechanical properties of fluid between the PIV and original models [Kumar, Acharya, Beuerman et al. (2006)]. In order to ensure the similarity of AH flows between the two models, similitude theory was conducted to get the same Reynolds number (Re) [Hong, Ji, Kim et al. (2017)]. Re was calculated according to Eq. (1):

$$Re_m = Re \text{ i. e. } \frac{\rho_m U_m d_m}{\mu_m} = \frac{\rho U d}{\mu} \quad (1)$$

where Re stand for Reynolds number, ρ was the fluid density, U was the local stream velocity, d was the reference diameter, μ was the fluid viscosity. The parameters of flow in the PIV model were represented by a subscript m while those in the original model had no subscript. U could be calculated with Eq. (2) according to the volumetric flux of AH secreted by ciliary body.

$$Q = \frac{1}{4} \pi d^2 U \quad (2)$$

Previous study has shown that AH was generated at a rate of about 3 $\mu\text{L}/\text{min}$ [Barocas and Huang (2004)]. Based on the similarity theory, an inlet rate of 15 $\mu\text{L}/\text{min}$ was selected to simulate AH generation in the PIV model. The details of model geometry, fluid properties, and similitude parameters in the PIV and original models are shown in Tab. 1.

Table 1: Geometry, fluid properties, and similitude parameters of the PIV and original models

Quantity	PIV model	Original model	Sources
Scaling factor	5	1	
Diameter of the anterior chamber D_C	65 mm	13 mm	[Repetto, Pralits, Siggers et al. (2015)]
Maximum height of chamber h_C	13.15 mm	2.63 mm	[Repetto, Pralits, Siggers et al. (2015)]
Maximum radius of curvature of the posterior cornea R_C	30.0 mm	6.8 mm	[Repetto, Pralits, Siggers et al. (2015)]
Radius of curvature of the natural lens R_L	50 mm	10 mm	[Repetto, Pralits, Siggers et al. (2015)]
Height of the iris–lens channel	0.5 mm	0.1 mm	[Repetto, Pralits, Siggers et al. (2015)]
Angle between cornea and iris	30°	30°	[Repetto, Pralits, Hasballa et al. (2015)]
AH density ρ	1000 kg·m ⁻³	1000 kg·m ⁻³	[Villamarin, Roy, Siggers et al. (2012)]
AH Viscosity μ	0.001 kg ⁻¹ s ⁻¹	0.001 kg ⁻¹ s ⁻¹	[Kumar, Acharya, Beuerman et al.(2006)]
AH volumetric flux secreted by ciliary body Q	15 μ L/min	3 μ L/min	[Barocas and Huang (2004)]

2.3 Differential pressure simulation

In this study, two different sets of driven mechanism for AH flow in anterior segment were considered: one was the production and drainage of AH, and the other was the differential pressure between AC and PC [Silver and Quigley (2004)]. The material of PIV model made from 3D printing was rigid, and it was different from that of real eyes. Meanwhile, it was difficult to install and operate a small-scale pressure control system in a small PIV model. The work of pressure for incompressible flow could be converted into kinetic energy based on the conservation of energy equation (Eq. (3)):

$$F \cdot h = \frac{1}{2}mv^2 \tag{3}$$

where F was stress, h was height, m and v represented quality and velocity. Therefore, we set various flow rates to simulate different differential pressure between AC and PC. It is

known that stress (F) is the multiplication of pressure (Δp) and area (s). Quality (m) can be calculated by density (ρ) and volume (V). Therefore, Eq. (3) can be described as:

$$\Delta p \cdot s \cdot h = \frac{1}{2} \rho V v^2 \quad (4)$$

Considering that volume (V) can be obtained by the multiplication of area (s) and height (h), Eq. (4) can be written as:

$$\Delta p = \frac{1}{2} \rho v^2 \quad (5)$$

Based on the data of differential pressures between AC and PC in our previous study [Song, Yang and Liu (2011)], the velocity corresponding to each pressure value can be calculated according to Eq. (5), which is shown in Tab. 2. Considering that the flow rate of simulation of AH generation was 15 $\mu\text{L}/\text{min}$, the inflow volumetric flow rates were set 115 $\mu\text{L}/\text{min}$, 260 $\mu\text{L}/\text{min}$ and 430 $\mu\text{L}/\text{min}$. The same flow rates were set under the condition of pupillary block. A low flow rate of 10 $\mu\text{L}/\text{min}$ was chose to conduct PIV experiment to verify the reliability and validity PIV result obtained at the higher rates.

Table 2: Equivalent volumetric flux of various differential pressures between AC and PC

Parameter	Value (Pa)	Equivalent volumetric flux ($\mu\text{L}/\text{min}$)
Maximum differential pressure	96.84	415
Minimum differential pressure	5.83	100
Average differential pressure	33.6	245

2.4 Experimental setup

Due to that the corneal surface was spherical, a square water tank filled with water was used so as to avoid the effect of refraction on the corneal surface [Yang, Song, Mei et al. (2013)]. Considering the extremely low flow rate (115-430 $\mu\text{L}/\text{min}$) in the experiment, it was necessary to choose proper tracer particles to ensure the following performance [Mei (1996)]. The PIV fluid and particle characteristics were shown in the Tab. 3.

Table 3: Detailed properties of tracer particles

Parameter	Units	Value
Seeding particle material	-	Polystyrene
Seeding particle mean diameter	μm	3.2
Seeding particle density	g/cm^3	1.05
Excitation wavelength	nm	538
Emission wavelength	nm	584

The diagram of PIV was shown in Fig. 3. Time-resolved measurements of flow field and real-time flow visualization were achieved by using high frame rate cameras and pulse rate lasers. A microinjection pump (PHD UT, Harvard instrument) was used to produce stable fluid flow at the inlet. PIV experiment included four steps. Firstly, the tracer

particle solution was injected into the model slowly and uniformly at room temperature. The injection lasted for 8 hours to guarantee a fully developed and non-turbulent flow pattern. No bubble entered the model and test circuit during injection to avoid potential reflections and shadows in PIV images [Raffel, Willert, Scarano et al. (2007)]. Then a low-frequency scintillating green laser (Beam. Optro. Ltd.) was used to illuminate the tracer particles. The laser passed through a cylindrical-like lens and was imaged by a digital camera with a 60 mm Micro-Nikkor lens. After that, the laser sheet (thickness <1 mm) was emitted into the central plane of PIV model and camera to reduce optical distortion and refraction. The laser sheet and camera were absolutely perpendicular during the whole experiment. Finally, after calibrating with a centimeter ruler, the light reflected by the particles (with wavelength more than 579 nm) was selected by a filter and was captured by the camera.

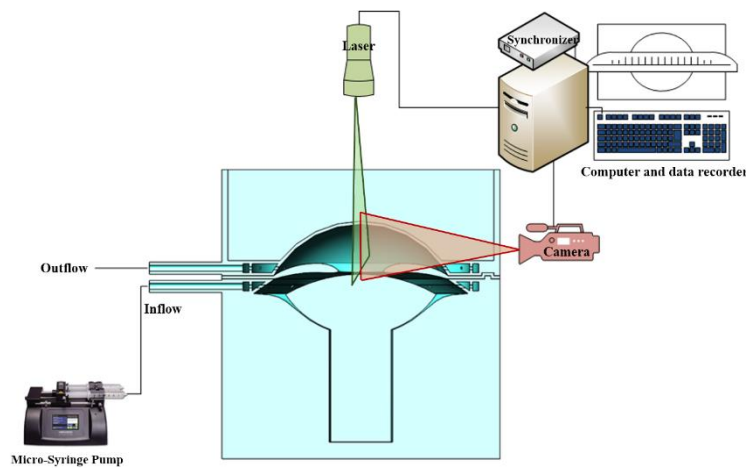


Figure 3: Diagram of PIV experiment

The commercial PIV platform Insight 4G was used to calculate the movement of the tracer particles. The size of window domain was 32×32 pixels, resulting in 2-9 particles in each domain. The sampling frequency of the image was 2 Hz, and the spatial resolution of the image was 640×480 pixels. Each particle occupied about 2-3 pixels, and its gray value was more than 200. After acquisition and computation of PIV data, velocity vectors, streamlines and vorticities of fluid flow were obtained by using TECPLOT image processing tool. Z-vorticity component was selected to evaluate the shear stress in fluid flow.

3 Results

The PIV image was calibrated using a centimeter scale (Fig. 4(a)). As shown in Fig. 4(b), the tracer particles were highly dispersed in the AC of the PIV model. These particles with different sizes could be accurately identified after gray processing. This indicated that experimental operation and particle properties could visualize the fluid flow effectively. The velocity vectors and streamlines in the AC at the inlet volumetric rate of

10 $\mu\text{L}/\text{min}$ was shown in Fig. 4(c) clearly, indicating the high reliability and validity of results under higher rates.

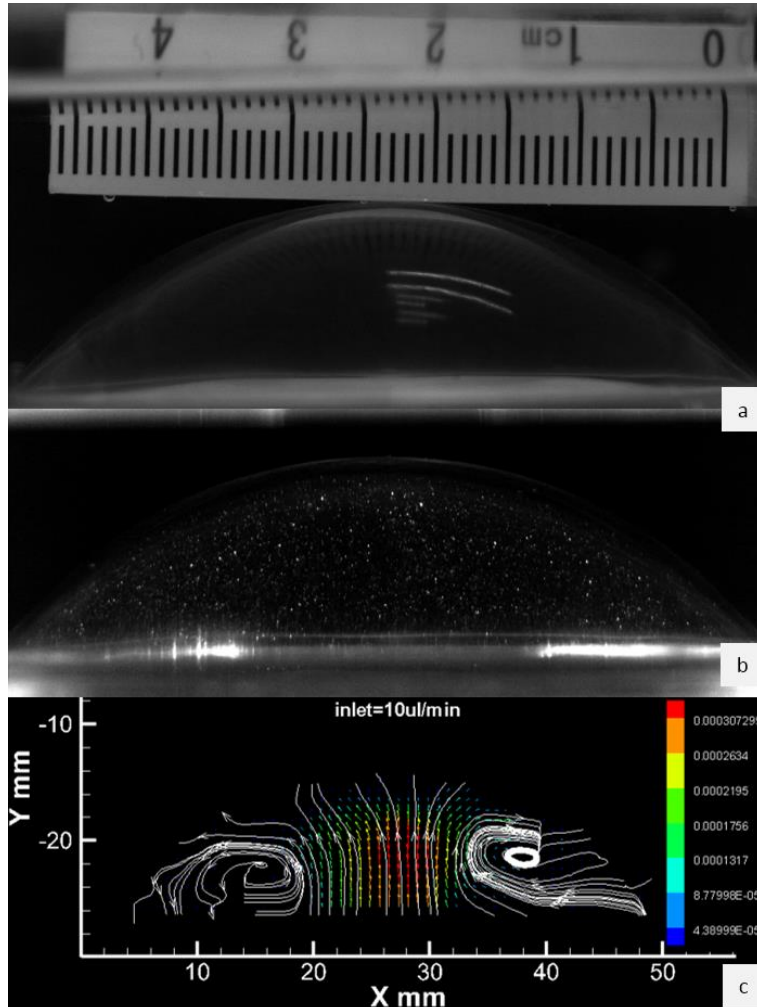


Figure 4: Calibration (a) and the tracer particles distribution (b) in the PIV image. Velocity vectors (m/s) and streamlines of AH flow (c) in AC at the rate of 10 $\mu\text{L}/\text{min}$

Fig. 5 reveals the velocity vectors and streamlines of fluid in the AC region of the PIV model under the normal condition (i.t. without pupillary block). As shown in Fig. 5(a), the streamlines were almost symmetrical in the flow field under the simulated condition of AH generation. The main flux occurred along the axes that connected pupil and AC angle. The fluid in AC flowed towards the cornea, descended along the cornea curvature and down to the irido-corneal angle. Around this direction, the velocity profiles changed, indicating the acceleration and deceleration of fluid. The fluid was discharged through the drainage channel eventually and two small-scale vortices could be observed. When the differential pressure between AC and PC was 5.83 Pa, the regions of the two vortices

increased obviously and were symmetric based on the sagittal plane of the AC (X-Y plane), which were marked with red arrows in Fig. 5(b). The velocity vectors and streamlines under the other pressures are shown in Fig. 5(c-d). It was found that the position of the maximum velocity (max-velocity) varied with the value of pressure. When the differential pressure was 5.83 Pa, a higher speed was achieved in the mid-portion of the AC. When the pressure became more than 33.6 Pa, the high speeds transferred to the surface of the iris and lens. This phenomenon indicated that the pressure had great influence on the flow filed in the AC. However, the max-velocity was 1.71×10^{-5} m/s, 1.54×10^{-5} m/s, and 2.01×10^{-5} m/s under three different pressure (Tab. 4), suggesting the max-velocity was less susceptible to the pressure.

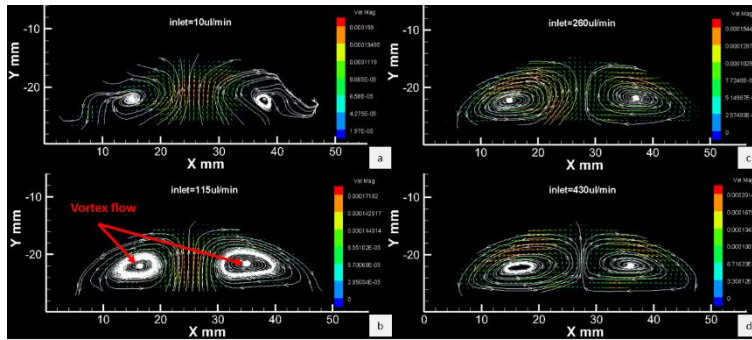


Figure 5: Velocity vectors (m/s) and streamlines of AH flow in the AC at various volumetric flux (a: 15; b: 115; c: 260; d: 430 $\mu\text{L}/\text{min}$) under the normal condition. X and Y represent the position of AC in image

Fig. 6 shows the vorticity (z-component) under the normal condition. As mentioned above, when the differential pressure between AC and PC appeared, two vortical zones with different directions were formed in the AC and they were symmetric in the X-Y plane. The higher levels of vorticity mainly occurred near the central corneal and the iris epithelium. With the increase of differential pressure, the vortex region became flat and extended near the cornea. Furthermore, the maximum vorticity (max-vorticity for short) increased with the differential pressure. When the pressure difference was 5.83 Pa, the max-vorticity was only $7.67 \times 10^{-5} \text{ s}^{-1}$. However, the max-vorticity achieved to $12.5 \times 10^{-5} \text{ s}^{-1}$ when the differential pressure increased to 96.84 Pa. These phenomena suggested an obvious effect of differential pressure on the vortical zones. Moreover, a shorter distance between the centers of two vortexes could be observed at the higher differential pressure. The distance decreased from 20.50 mm at 5.83 Pa to 19.64 mm at 33.5 Pa and became 15.41 mm at 96.84 Pa (Tab. 4).

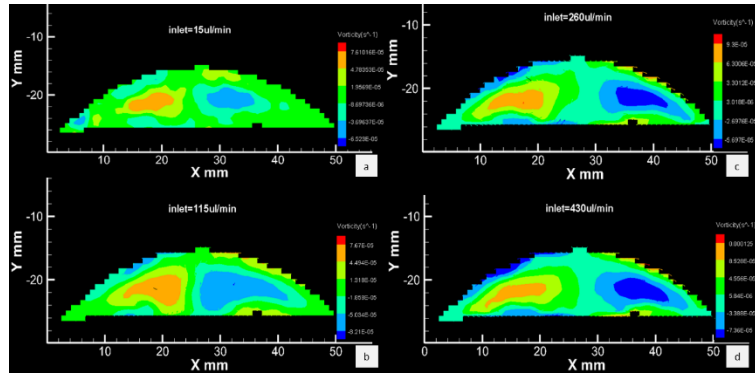


Figure 6: Z-component of vorticity (s^{-1}) of AH flow in the AC at various volumetric flux (a: 15; b: 115; c: 260; d: 430 $\mu L/min$) under the normal condition. X and Y represent the position of AC in image

Table 4: The maximum velocity and the distance between the two vortex cores in AC at various differential pressure between AC and PC

Differential pressure (Pa)	Max-velocity (10^{-4} m/s)	Max-vorticity (10^{-5} s^{-1})	Distance between vortex cores (mm)
0	1.58	7.61	22.86
5.83	1.71	7.67	20.50
33.5	1.54	9.30	19.64
96.84	2.01	12.50	15.41

The velocity vectors and streamlines in the AC under the condition of pupillary block are shown in Fig. 7. Comparing with the results under the normal condition, the flow pattern was obviously asymmetric when the pupillary block occurred. The main flux centered in the left side of the pupil. Notably, higher velocity appeared in the left side while much lower velocity in the right side (Fig. 7(a)). When the differential pressure between AC and PC appeared, two asymmetry vortexes could be observed (Fig. 7(b-d)). The small one located near the AC angle while the other in the middle area. Pupillary block also changed the location of max-velocity obviously. At the differential pressure of 5.83 Pa, the max-velocity appeared in the middle area of AC under the normal condition while near the iris and central area of cornea under the condition of pupillary block. Besides, the vorticity (z-component) also varied greatly when the pupillary block occurred. The two vortical zones became asymmetric and the position of the vortex cores also varied (Fig. 8(a)). Furthermore, the higher level of vorticity transferred to the central area between iris and cornea at all the differential pressure (Fig. 8(b-d)). These phenomena suggested that the occurrence of pupillary block had a great effect on the fluid dynamic in AC, which might further damage the eye health and vision.

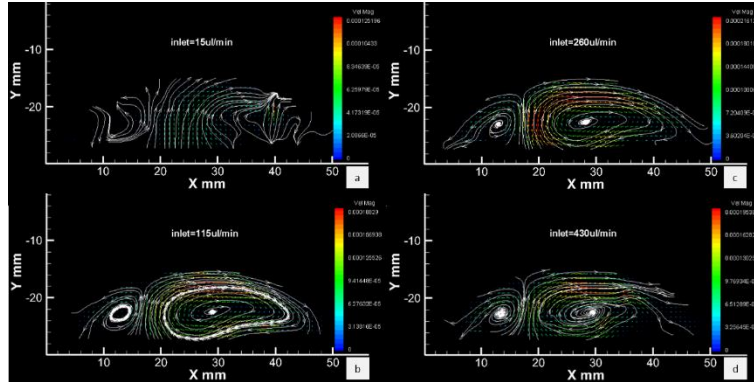


Figure 7: Velocity vectors (m/s) and streamlines of AH flow in the AC at various volumetric flux (a: 15; b: 115; c: 260; d: 430 $\mu\text{L}/\text{min}$) under the condition of pupillary block. X and Y represent the position of AC in image

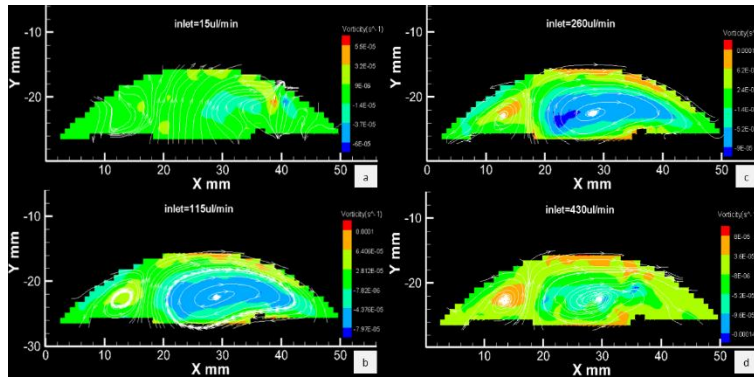


Figure 8: Z-component of vorticity (s^{-1}) of AH flow in the AC at various volumetric flux (a: 15; b: 115; c: 260; d: 430 $\mu\text{L}/\text{min}$) under the condition of pupillary block. X and Y represent the position of AC in image

4 Discussion

In this study, PIV combined with 3D printing technology was used to investigate the AH flow and distribution in eyes and the potential risks of pupillary block. A transparent eye model with high spatial resolution was designed and used for PIV experiments. Results demonstrated the feasibility of PIV combined with 3D printing for AH flow simulation and visualized the fluid flow in the AC at low velocity. Besides, the PIV model could be disassembled and rinsed by the deionized water due to its modular design, which avoided the accumulation and adhesion of fluorescent particles in the model [Schlanstein, Hesselmann, Jansen et al. (2015)]. Moreover, the model could simulate the generation of AH accurately and maintain a steady differential pressure between AC and PC at various levels, which was difficult to achieve in real eyes.

The results of PIV revealed the flow of AH clearly. Under the normal condition, AH flowed out of pupil and into inner surface of cornea, then fell along corneal curvature,

and finally drained through the AC angle, which were accorded with a previous study [Villamarin, Roy, Hasballa et al. (2012)]. By simulating various differential pressures between AC and PC, an obvious change in the position of max-velocity could be observed. The max-velocity shifted near the corneal endothelium and iris epithelium when the differential pressure exceeded 33.6 Pa, which might damage the central corneal endothelial cell. The occurrence of pupillary block could cause an obvious disturbance on the flow distribution. The flow of AH was restricted by the blocked area between iris and lens, resulting in a narrower gap between iris and lens as well as higher vorticity near iris [Dvoriashyna, Repetto, Romano et al. (2017)], which might influence the mechanical characteristics of iris and further increase the risk of iris bomb [Dvoriashyna, Repetto, Romano et al. (2017); Mapstone (1968)]. Furthermore, pupil block also changed the position of stagnation point in AC, which might lead to a lack of nutrition in the central cornea.

Our results demonstrated that the vorticity field in AC region changed obviously after the pupillary block. The vorticity in the z direction, representing the shear rate, transferred near the regions of paracentral cornea and iris epithelium. It is known that shear stress is proportional to shear rate according to Newton's law for viscous fluid. Therefore, it could be induced that the shear stresses in these regions would increase due to pupillary block. Shear stress is crucial for transporting messages between cells as well as cell disruption [Liang, Slattery and Dong (2005)]. Previous study has demonstrated that the number of detached corneal endothelial cells increased with the shear stresses applied [Kaji, Oshika, Usui et al. (2005)]. Considering that the patients with PACG have the corneal endothelial cell density smaller than normal [Korey, Gieser, Kass et al. (1982); Hong, Kandori, Kitazawa et al. (1982); Malaise-Stals, Collignon-Brach and Weekers (1984); Gagnon, Boisjoly, Brunette et al. (1997)], it may be due to that the occurrence of pupillary block disrupts the flow in pupil, resulting in greater shear stress in the corresponding field (e.g. paracentral cornea and the iris epithelium in this study), thereby increasing the risk of corneal endothelial cells detachment.

However, the PIV model still has some limitations and requires further study. Slight asymmetry could be observed in the flow field under the normal condition, which might be due to the assembly deviations. Furthermore, the quality of PIV image in AC angle can be further improved by increasing the translucency of drainage channels in the model. Future study will further optimize the model structure and assembly process, and try to verify the results by in-vivo PIV.

5 Conclusions

In this study, the hydrodynamics of AH flow in AC under the condition of various differential pressures between AC and PC and in the situation of pupillary block were assessed by using 3D printing and PIV technique. The results obtained by PIV experiment demonstrated that elevated differential pressure as well as pupillary block would disturb the AH flow obviously. When the differential pressures exceeded 33.6 Pa, the flow velocity near the corneal endothelium and iris epithelium increased greatly, which might damage the endothelial cells in these regions. The occurrence of pupillary block could increase the shear stress in the paracentral cornea and iris epithelium, which might cause the incidence of PACG. Our research demonstrated the feasibility of

low-speed AH flow visualization and evaluated the potential risks of glaucoma due to pupillary block, which provided a scientific basis for further study of PACG pathogenesis.

Data availability

The data used to support the findings of this study are available from the corresponding author upon request.

Conflict of interest

The authors declare that there is no conflict of interest regarding the publication of this paper.

Ethical Approval

Not required

Acknowledgements: This research was funded by the National Natural Science Foundation of China [31570952, 10802053]; Beijing Natural Science Foundation [7152022]. The authors would like to acknowledge the assistance of the PIV system in Beijing University of Technology and acknowledge the National Eye Institute (Bethesda, Maryland) as the source for Fig. 1.

References

Avtar, R.; Srivastava, S. (2014): The convection flow of aqueous humor in the anterior chamber of human eye. *Advances in Applied Science Research*, vol. 5, pp. 359-369.

Aycock, K. I.; Hariharan, P.; Craven, B. A. (2017): Particle image velocimetry measurements in an anatomical vascular model fabricated using inkjet 3D printing. *Experiments in Fluids*, vol. 58, pp. 154.

Barkan, O. (1954): Narrow-Angle Glaucoma: Pupillary Block and the Narrow-Angle Mechanism. *American Journal of Ophthalmology*, vol. 37, pp. 332-350.

Barocas, V. H.; Huang, E. C. (2004): Aqueous humor and iris mechanics in pupillary block and primary angle-closure glaucoma. *Investigative Ophthalmology & Visual Science*, vol. 45, pp. 5033.

Caprioli, J. (1992): The ciliary epithelia and aqueous humor. *Adlers Physiology of the Eye*, pp. 228.

Chan, E. W. E.; Li, X.; Tham, Y. C.; Liao, J.; Wong, T. Y. et al. (2016): Glaucoma in Asia: regional prevalence variations and future projections. *British Journal of Ophthalmology*, vol. 100, pp. 78-85.

Congdon, N. G.; Friedman, D. S. (2003): Angle-closure glaucoma: impact, etiology, diagnosis, and treatment. *Current Opinion in Ophthalmology*, vol. 14, pp. 70-73.

Dvoriashyna, M.; Repetto, R.; Romano, M. R.; Tweedy, J. H. (2017): Aqueous humour flow in the posterior chamber of the eye and its modifications due to pupillary block and iridotomy. *Mathematical Medicine and Biology-Journal of the IMA*, pp. 1-21.

Ethier, C. R.; Johnson, M.; Ruberti, J. (2004): Ocular biomechanics and biotransport. *Annual Review of Biomedical Engineering*, vol. 6, pp. 249-273.

Fontana, S. T.; Brubaker, R. F. (1980): Volume and depth of the anterior chamber in the normal aging human eye. *Archives of Ophthalmology*, vol. 98, pp. 1803-1808.

Gagnon, M. M.; Boisjoly, H. M.; Brunette, I.; Charest, M.; Amyot, M. (1997): Corneal endothelial cell density in glaucoma. *Cornea*, vol. 16, pp. 314-318.

Hong, C.; Kandori, T.; Kitazawa, Y.; Tanishima, T. (1982): The corneal endothelial cells in ocular hypertension. *Japanese Journal of Ophthalmology*, vol. 26, pp.183-189.

Hong, H.; Ji, H. S.; Kim, H. D.; Kim, K. C. (2017): Temporal and spatial flow structures in a simulated vessel with stenotic lesion using time-resolved PIV technique. *Journal of Vision*, vol. 20, pp. 833-845.

Huang, A. S.; Francis, B. A.; Weinreb, R. N. (2017): Structural and functional imaging of aqueous humor outflow: a review. *Clinical and Experimental Ophthalmology*, vol. 46, pp. 158-168.

Huang, E. C.; Barocas, V. H. (2004): Active iris mechanics and pupillary block: Steady-state analysis and comparison with anatomical risk factors. *Annual Review of Biomedical Engineering*, vol. 32, pp. 1276-1285.

Kaesler, A.; Schlanstein, P. C.; Hesselmann, F.; Büsen, M.; Klaas, M. et al. (2017): Experimental approach to visualize flow in a stacked hollow fiber bundle of an artificial lung with particle image velocimetry. *Artificial Organs*, vol. 41, pp. 529-538.

Kaji, Y.; Oshika, T.; Usui, T.; Sakakibara, J. (2005): Effect of shear stress on attachment of corneal endothelial cells in association with corneal endothelial cell loss after laser iridotomy. *Cornea*, vol. 24, pp. 55-58.

Korey, M.; Gieser, D.; Kass, M. A.; Waltman, S. R.; Gordon, M. et al. (1982): Central corneal endothelial cell density and central corneal thickness in ocular hypertension and primary open-angle glaucoma. *American Journal of Ophthalmology*, vol. 94, pp. 610-616.

Kumar, S.; Acharya, S.; Beurman, R.; Palkama, A. (2006): Numerical solution of ocular fluid dynamics in a rabbit eye: parametric effects. *Annals of Biomedical Engineering*, vol. 34, pp. 530-544.

Liang, S.; Slattery, M. J.; Dong, C. (2005): Shear stress and shear rate differentially affect the multi-step process of leukocyte-facilitated melanoma adhesion. *Experimental Cell Research*, vol. 310, pp. 282-292.

Malaise-Stals, J.; Collignon-Brach, J.; Weekers, J. F. (1984): Corneal endothelial cell density in acute angle-closure glaucoma. *Ophthalmologica*, vol. 189, pp. 104-109.

Mapstone, R. (1968): Mechanics of pupil block. *British Journal of Ophthalmology*, vol. 52, pp. 19.

Mei, R. (1996): Velocity fidelity of flow tracer particles. *Experiments in Fluids*, vol. 22, pp. 1-13.

National Eye Institute. (2012): Drawing of the eye.

<https://www.flickr.com/photos/nationaleyeinstitute/sets/72157646829197286>

Olkhovskiy, V.; Friedmann, E. (2017): Development and simulation of the aqueous humor flow in the anterior chamber. *Topical Problems of Fluid Mechanics*, pp. 241-248.

Pascolini, D.; Mariotti, S. P. (2012): Global estimates of visual impairment: 2010. *British Journal of Ophthalmology*, vol. 96, pp. 614-618.

Quigley, H. A.; Friedman, D. S.; Congdon, N. G. (2003): Possible mechanisms of primary angle-closure and malignant glaucoma. *Journal of Glaucoma*, vol. 12, pp. 167-180.

Raffel, M.; Willert, C. E.; Scarano, F.; Kahler, C. J.; Wereley, S. T. et al. (2007): *Particle Image Velocimetry: A Practical Guide. 2th ed.* Berlin: Springer.

Repetto, R.; Pralits, J. O.; Siggers, J. H.; Soleri, P. (2015): Phakic iris-fixated intraocular lens placement in the anterior chamber: effects on aqueous flow. *Investigative Pphthalmology & Visual Science*, vol. 56, pp. 3061-3068.

Scardulla, F.; Bellavia, D.; D'Acquisto, L.; Raffa, GM.; Pasta, S. (2017): Particle image velocimetry study of the celiac trunk hemodynamic induced by continuous-flow left ventricular assist device. *Medical Engineering & Physics*, vol. 47, pp. 47-54.

Schlanstein, P. C.; Hesselmann, F.; Jansen, S. V.; Gemsa, J.; Kaufmann, T. A. et al. (2015): Particle image velocimetry used to qualitatively validate computational fluid dynamic simulations in an oxygenator: a proof of concept. *Cardiovascular Engineering and Technology*, vol. 6, pp. 340-351.

Sena, D. F.; Lindsley, K. (2013): Neuroprotection for treatment of glaucoma in adults. *Cochrane Database Syst Rev*, CD006539.

Silver, D. M.; Quigley, H. A. (2004): Aqueous flow through the iris-lens channel: estimates of differential pressure between the anterior and posterior chambers. *Journal of Glaucoma*, vol. 13, pp. 100-107.

Song, H. F.; Yang, H. Y.; Liu, Z. C. (2011): Surveying of pressure in posterior chamber and pressure difference between anterior and posterior chambers of rabbit eye *in vivo*. *Beijing Biomedical Engineering*, vol. 30, pp. 335-338.

Tham, Y. C.; Hons, B. S.; Li, X.; Wong, T. Y.; Quigley, H. A. et al. (2014): Global prevalence of glaucoma and projections of glaucoma burden through 2040: a systematic review and meta-analysis. *Ophthalmology*, vol. 121, pp. 2081-2090.

Villamarin, A.; Roy, S.; Hasbala, R.; Vardoulis, O.; Reymond, P. et al. (2012): 3D simulation of the aqueous flow in the human eye. *Medical Engineering & Physics*, vol. 34, pp. 1462-1470.

Wang, W. J.; Qian, X. Q.; Song, H. F.; Zhang, M. D.; Liu, Z. C. (2016): Fluid and structure coupling analysis of the interaction between aqueous humor and iris. *Biomedical Engineering Online*, vol. 15, no. 2, pp. 133.

Weinreb, R. N.; Aung, T.; Medeiros, F. A. (2014): The pathophysiology and treatment of glaucoma: a review. *Journal of the American Medical Association*, vol. 311, pp. 1901-1911.

Wessapan, T.; Rattanadecho, P. (2014): Aqueous humor natural convection of the human eye induced by electromagnetic fields: in the supine position. *Journal of Medical and Bioengineering*, vol. 3, pp. 251-258.

Yang, H. Y.; Song, H. F.; Mei, X.; Li, L.; Fu, X. N. et al. (2013): Experimental research on intraocular aqueous flow by PIV method. *Biomedical Engineering Online*, vol. 12, pp. 108.